Open Access Online Journal on Astronomy and Astrophysics

Acta Astrophysica Taurica

www.astrophysicatauricum.org

Acta Astrophys. Tau. 5(3), 6–13 (2024)

Spatial and temporal features of the behavior of microwave and ultraviolet emission in eruptive events

I.A. Bakunina[1], V.F. Melnikov[2], A.V. Shain[2], V.E. Abramov-Maximov[2], A.S. Morgachev[3]

[1] HSE University, Bolshaya Pecherskaya 25/12, Nizhny Novgorod 603155, Russia
e-mail: rinbak@mail.ru
[2] Central Astronomical Observatory at Pulkovo of RAS, Pulkovskoe shosse 65/1, St. Petersburg 196140, Russia
[3] Lobachevsky State University of Nizhny Novgorod, prospekt Gagarina 23, Nizhny Novgorod 603022, Russia

Received 1 November 2021

ABSTRACT

Observational signatures that determine the ability of a solar active region to cause a mass ejection into the high layers of the solar corona (CME) are not entirely clear to date. This makes it difficult to understand the physical mechanism of the CME trigger. This paper presents a search for observational signatures that may indicate the emergence of an eruptive process. For this aim, we have carried out a comparative analysis of the conditions before and during a flare for flare events both accompanied and not accompanied by CMEs. We studied the features of the spatial and temporal dynamics of microwave and ultraviolet emission (data from the Nobeyama Radio Heliograph, SDO/AIA), as well as magnetic fields (SDO/HMI) for 16 active regions (ARs). Using this sample, it was found that the flares accompanied by CMEs most often occur in open magnetic configurations, in regions with twisted magnetic ropes and emerging magnetic fluxes. CMEs are also observed most often in flares of longer duration and in those ARs that have sources in microwave radiation that are more extended in area.

Key words: Sun, solar flares, coronal mass ejections, microwave emission, ultraviolet emission

1 Introduction

An important task in solar activity research is searching for theoretical and observational signatures that determine the ability of an active region (AR) to cause an eruption of matter into the high layers of the solar corona. Currently, there are many ideas and models explaining the mechanism of eruptions in active regions and subsequent coronal mass ejections (CMEs). The most well-known of them, the so-called Standard Flare Model, or CSHKP model (Carmichael, 1964; Sturrock, 1966; Hirayama, 1974; Kopp and Pneuman, 1976), suggests the presence of magnetic flux ropes (MFRs) in the corona of ARs as a prerequisite for initiating eruptive flares. An MFR is recognized as a set of magnetic field lines twisted around a central axis more than once (Gibson et al., 2006). However, the exact mechanism of magnetic flux rope formation is still unclear and controversial. Their formation is usually associated with a) the emergence of twisted magnetic flux ropes and their long-term (days or more) existence under magnetic arcades (see, for example, Solov'ev, 2021) and also b) the accumulation of magnetic energy in the polarity inversion line (PIL) region as a result of sunspot rotation in the AR and/or relative shear of the photospheric layers along the PIL. Flux ropes are believed to form as a result of flux reconnection along the PIL (van Ballegooijen and Martens, 1989).

Using observations, MFRs have been identified in the form of various solar features, such as filaments, filament channels, hot coronal channels, and coronal sigmoids. While filaments and filament channels are observed in chromospheric absorption lines, sigmoids and hot channels are observed in emission line details of the solar corona. Sigmoids are S-shaped (or inverse S-shaped) structures observed in soft X-ray (SXR) and extreme ultraviolet (EUV) images of the Sun (Rust and Kumar, 1996; Manoharan et al., 1996). Filaments and hot channels are different observational manifestations of MFRs lying at chromospheric and coronal heights, respectively (Cheng et al., 2014a, b). However, the most important feature of hot channels and coronal sigmoids is their frequent association with CMEs, which has been presented in several studies and statistical reviews (see, for example, Canfield et al., 1999, 2007; Nindos et al., 2015). Emerging magnetic fluxes are not always a necessary condition for eruptive flares (Romano et al., 2015). The decisive factor is the monotonic increase in magnetic helicity accumulated in the corona. That is, shear motions bring more magnetic energy into subsequent eruptive events than emerging fluxes.

Previously, in our works (Bakunina and Melnikov, 2019; Bakunina et al., 2020a, b), we investigated eruptive and non-eruptive (without CMEs) M-class flares. We found the appearance of bright and "hot" ($T \sim 10^7 K$) loops in the EUV range (94 and 131 Å) crossing each other a few hours before

the flares, which we called X-structures. It is in this place that the flare is then initiated. We also found that the maximum in the radio emission intensity at a frequency of 17 GHz (NoRH data) spatially coincides with the X-structure, and strong nonstationarity in the behavior of radio emission is observed before the flare.

It is known that an AR or a specific flare in it can be eruptive, but no CME occurs, and then these events are usually called confined in the literature. Here, confusion arises with the use of the term "non-eruptive" flare. In the following, we will use the NOAA flare catalog, Space Weather Prediction Center (SWPC), and divide flares into confined (C) and flares with CMEs (E). But those confined flares where an eruption is noted in the catalog will be marked with the CE symbol.

This work aims to continue the search for differences between events with CMEs and confined events based on a sample of 16 ARs, which also includes the events previously studied in detail by us.

2 Observations

2.1 Observational data and processing method

The analysis of the spatial dynamics of microwave emission from active regions was performed using solar radio maps obtained by the Nobeyama Radio Heliograph (NoRH) at a frequency of 17 GHz with a two-dimensional spatial resolution of 10″–15″, with a time interval between images of 10 minutes and 3 minutes, and based on observational data from SDO/AIA in the EUV range of 94 and 131 Å with a spatial resolution of ~ 1.5″, as well as observational data of the photospheric magnetic field from SDO/HMI. For the nonlinear force-free extrapolation of magnetic fields into the AR corona, we used the algorithms presented in Wiegelmann (2004) and the software available on GitHub developed by S.A. Anfinogentov[5] and A.G. Stupishin[6].

We investigated 16 ARs in the pre-flare phase before confined (C) events, confined events with eruption (CE) (a total of 8), and events with CMEs (E) (a total of 8). Of these, 11 flares were selected from Duan et al. (2019) and previously studied by us (Bakunina et al., 2021). All events belong to the period of 2011–2017. The sample included only those events whose observation time fell within the observation interval of NoRH (22:50–06:20 UT). We also investigated only M-class X-ray flares (GOES). Table 1 presents the parameters of the flares and the observational signatures that, in our opinion, may be significant in predicting the possibility of a CME event (the last four columns).

The first, second, and third columns of Table 1 show the data on the date, time of the flare in radio emission (according to NoRH data), and its X-ray class, respectively. The rightmost column contains the characteristic area of the radio source at a frequency of 17 GHz in arcsec^2 (when approximated by a rectangle, measured in pixels, then multiplied by 25 (pixel area 4.9″ × 4.9″)). The measurement errors of the radio source areas are determined by the half-width of the beam pattern (~ 5″–10″ at 17 GHz) and on average amount to about 15–20 % or less of the radio source area.

The second column in parentheses shows time of the flare peak according to SWPC (top row); below are the start time

[5] https://github.com/Sergey-Anfinogentov/GXBox_prep (accessed on October 15, 2021).

[6] https://github.com/Alexey-Stupishin/Magnetic-Field_Library (accessed on October 15, 2021)

Table 1. Main characteristics of the events selected for the study

Date	Flare time	Flare class	NOAA	Flare position	Flare position (above sunspot or near sunspot (S), in inter-spot zone (IS)	Event type	Presence of sigmoid	Emerging flux	Presence of open magnetic configurations	Area of radio source before flare (arcsec^2)
1	2	3	4	5	6	7	8	9	10	11
2011–07–30	(02:09) 02:07:22 02:07:55 02:17:16 D=10	M9.3	11261	N16E19	IS	C[1]	no	no	Present, trailing part of AR, there – CH[2]	15000
2011–10–02[3]	(00:50) 00:41:54 00:43:34 01:51:03 D=69	M3.9	11305	N09W12	S (southern part of sunspot)	CE	no	no	Present, northern part of sunspot	12500
2012–05–10	(04:18) 04:15:11 04:15:31 04:21:14 D=6	M5.7	11476	N13E22	IS	C	no	no	Present, trailing part of AR, there – CH	18750
2013–11–03	(05:22) 05:19:57 05:21:38 06:30:00 D=10	M5.0	11884	S12W16	IS	C	no	no	no	18750

Table 1. Continued

Date	Flare time	Flare class	NOAA	Flare position	Flare position (above sunspot or near sunspot (S), in inter-spot zone (IS))	Event type	Presence of sigmoid	Emerging flux	Presence of open magnetic configurations	Area of radio source before flare (arcsec^2)
1	2	3	4	5	6	7	8	9	10	11
2014–02–04	(04:00) 03:49:38 03:50:27 04:28:59 D=39	M5.2	11967	S14W06	S (left of trailing sunspot)	CE	yes	no	Present, leading part of AR	22500
2011–09–25	(02:33) 02:29:06 02:32:35 02:37:20 D=8	M4.4	11302	N13E48	IS	CE	no	no	Present, trailing zone, in trailing part – CH	30000
2014–10–22	(01:59) 01:17:41 01:39:12 03:25:43 D=128	M8.7	12192	S12E21	S (northern part of trailing sunspot)	C	yes	no	Present, southern part of trailing sunspot	30000
2017–09–04	(05:49) 05:37:18 05:39:15 06:29:59 D=52	M1.2	12673	S10W05	S (southern part of new sunspot)	CE	yes	yes	no	12500
2011–09–06	(01:50) 01:42:10 01:44:28 02:45:00 D=63	M5.3	11283	N14W07	S (leading)	E	no	no	Present, in leading part of AR, and near it there is CH	39375
2012–01–23	(03:59) 01:36:44 03:50:32 06:06:51 D=270	M8.7	11402	N28W21	IS (north of leading sunspot)	E	yes	yes	Present, (central part of AR, northern part	60000
2012–03–09	(03:53) 03:24:55 03:38:39 04:48:01 D=83	M6.3	11429	N15W03	No magneto-gram (anti-Hale)	E	yes	no	Present, in trailing part of AR – CH	45000
2013–10–24	(00:28) 00:26:05 00:27:56 00:43:27 D=17	M9.3	11877	S10E08	IS (Left and north of trailing sunspot, between AR 11877 and 11879)	E	no	yes	Present, but in leading part of AR	33750
2014–09–28[4]	(02:58) 02:32:35 02:43:10 03:24:33 D=53	M5.1	12173	S13W23	S (southern part), left of 12172 located)	E	yes	no	Present, trailing part of AR 12172 and southern part of AR 12173	30000
2014–12–17	(04:42) 04:03:11 04:32:08 06:29:59 D=146	M8.7	12242	S20E09	S (southern part)	E	yes	yes	Present, trailing part of AR	30000

Table 1. Continued

Date	Flare time	Flare class	NOAA	Flare position	Flare position (above sunspot or near sunspot (S), in inter-spot zone (IS)	Event type	Presence of sigmoid	Emerging flux	Presence of open magnetic configurations	Area of radio source before flare (arcsec^2)
1	2	3	4	5	6	7	8	9	10	11
2011–08–02	(06:19) 05:35:41 06:08:56 06:30:02 D=55	M1.4	11261	N17W10	S – left edge of trailing sunspot (open configu-ration)	E	no	no	Present, (trailing part and center of AR, left of trailing part – CH	35000
2015–06–21	(No PRF) 01:26:48 01:36:13 05:12:13 D=225	M2.6	12371	N13E14	No magneto-gram	E	yes	yes	Present, trailing part, near AR (leading part) there is CH	35000

T_{start}, peak time T_{peak}, and end time T_{end} of the flare at a frequency of 17 GHz (NoRH data); the last row in each cell is the duration of the flare (D) at a frequency of 17 GHz.

The sixth column shows the results of identifying the coordinates of the brightness peak in radio emission with the SDO/HMI magnetogram. The seventh column contains the types of events determined according to the SWPC flare catalog and the table published in Duan et al. (2019).

The eighth, ninth, and tenth columns of Table 1 use data from the Heliophysics Events Knowledgebase[7] (HEK). The presence of an open magnetic configuration in the AR and coronal holes near it can be considered from the images at 211, 193, and 171Å, superimposed on one map (images are available on SolarMonitor[8], the algorithm is on GitHub[9]).

2.2 Analysis of the parameters in Table 1

From the analysis of the second column of Table 1 for two subsamples of data, it can be concluded that events with CMEs have longer-lasting flares in radio emission at a frequency of 17 GHz. For clarity, the duration of flares in the radio range is presented in the form of histograms in Figs. 1 and 2.

It also follows from the last column of Table 1 that the areas of radio sources in the quiet phase are larger in events with CMEs. For clarity, this is shown in the diagrams of Figs. 3 and 4. As can be seen, the areas of radio sources for all events with CMEs clearly exceed 30000 arcsec^2, whereas for confined events, all areas are less than 30000 arcsec^2 (in two cases, they are equal to 30000 arcsec^2).

Thus, based on our data sample, we can conclude that events with CMEs are characterized, on average, by a longer flare duration and more extended radio sources than confined events, and, consequently, by more extensive systems of magnetic loops.

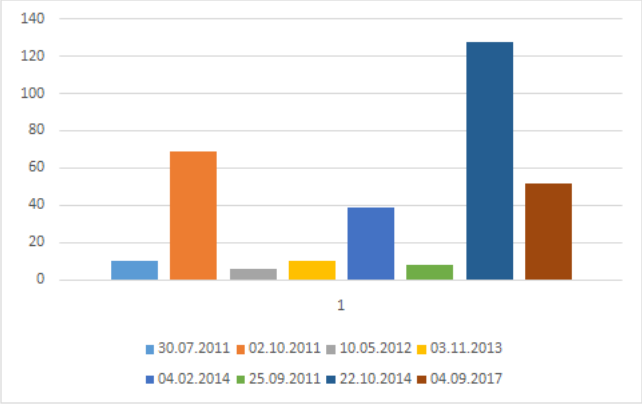

Fig. 1. Distribution diagram of flare durations (in minutes) at a frequency of 17 GHz for confined events. With the exception of two events out of eight, the flare duration does not exceed 60 minutes.

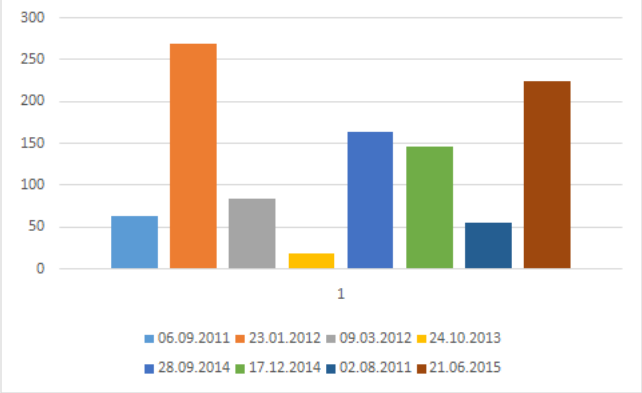

Fig. 2. Distribution diagram of flare durations (in minutes) at a frequency of 17 GHz for events with CMEs. With the exception of two events out of eight, the flare duration exceeds 60 minutes.

[7] https://www.lmsal.com/isolsearch
[8] https://www.solarmonitor.org/
[9] https://github.com/TCDSolar/CHIMERA

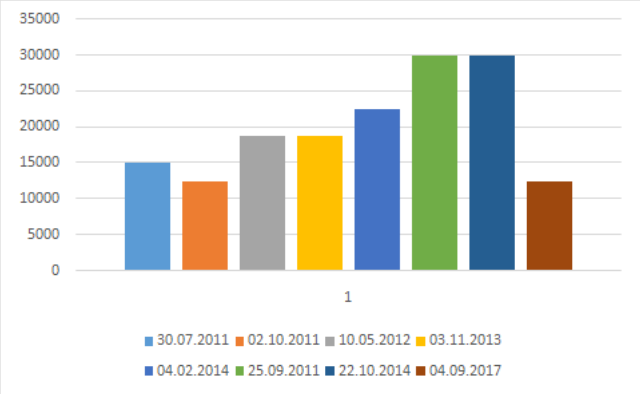

Fig. 3. Distribution diagram of the approximated area of radio sources in the pre-flare phase at a frequency of 17 GHz in arcsec^2 (vertical axis) for confined events.

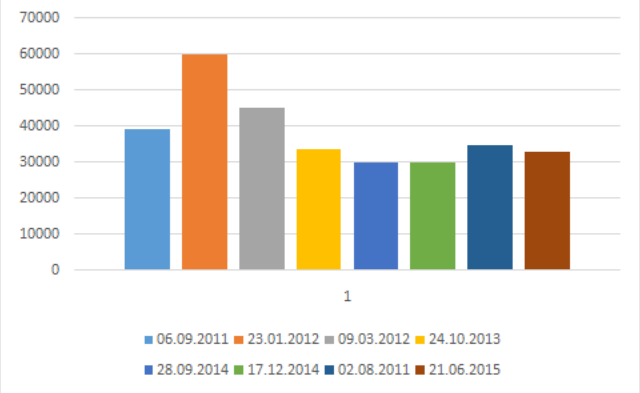

Fig. 4. Distribution diagram of the approximated area of radio sources in the pre-flare phase at a frequency of 17 GHz in arcsec^2 (vertical axis) for events with CMEs.

2.3 Analysis of the parameters in Table 1 (continued): Example of spatial dynamics of microwave and EUV emission

Analyzing the eighth and ninth columns of Table 1, we note that sigmoids are present in three out of eight confined events and in five out of eight events with CMEs. Emerging fluxes are present in one out of eight confined events and in four out of eight events with CMEs. Our sample is not very large, but it can still be concluded that emerging fluxes and sigmoids are more often recorded in events with CMEs.

As an illustration of the presence of a sigmoid, we provide an example of overlaying the contours of the distribution of intensity and circular polarization of radio emission (17 GHz) on two-dimensional SDO/AIA maps in EUV at 94 and 131 Å for an event with a CME in AR 11429 on March 9, 2012 (Figs. 5 and 6) before an M6.3 flare (T_{start} = 03:24:55, T_{peak} = 03:38:39, T_{end} = 04:48:01) and during the flare. We note that this is the only AR in our sample with an anti-Hale orientation of the magnetic field.

From the spatial dynamics presented in the images, we can see that approximately two hours before the onset of the flare, a crossed structure is observed in EUV, which coincides with the maximum radio brightness in intensity. At the same time, polarized microwave sources with different signs of circular polarization are observed at the ends of the sigmoid (left upper panel of Fig. 6). During the flare, a loop appears in radio emission, transverse to the sigmoid, possibly structurally associated with the eruption's escape beyond the magnetic field of the AR as a CME.

2.4 Analysis of the parameters in Table 1 (continued). The structure of the magnetic field at coronal heights

Analyzing the sixth and tenth columns of Table 1 together, it can be concluded that, in general, both for confined events and for events with CMEs, the presence of open magnetic configurations in one or another part of the AR and the presence of coronal holes near some ARs in both subsamples are characteristic. But in events with CMEs, the flare is localized near such open magnetic configurations (and coronal holes). In contrast, in confined events, the flare occurs either in the inter-spot zone or in those parts of the AR where there are no open magnetic structures and coronal holes; in both cases, a possible eruption is probably held inside the closed structure of the AR's magnetic field.

To illustrate this phenomenon, we performed a nonlinear force-free field (NLFFF) extrapolation of the magnetic fields into the AR corona for two events from the two subsamples using the algorithms specified in Sect. 2.1. One of the events is attributed to confined – an M4.9 flare that occurs in AR 11884 (03.11.2013), as can be seen from Table 1, in the inter-spot region in the absence of open magnetic configurations. The other event, an M5.1 flare (28.09.2014) accompanied by a CME, occurs in the open magnetic configuration in the southern part of AR 12173, adjacent to AR 12172.

Figure 7 shows the evolution of the magnetic field in AR 11884, ultraviolet (131 and 94 Å) and radio emission (17 GHz) in intensity before and during the M4.9 flare on November 3, 2013 (T_{start} = 05:19, T_{peak} = 05:21, T_{end} = 06:30 UT) without an eruption in a beta-gamma magnetic configuration. The upper panels show that 2–3 hours before the flare, between two neighboring sunspots connected by magnetic arches of field lines, directly under them and almost perpendicular to them, a powerful curved magnetic field rope formed (left and middle panels). It is here that the flare began, manifesting itself in the form of ignition of crossed EUV loops (right panel). The maximum brightness of radio emission in intensity at a frequency of 17 GHz also falls on this region (lower panel). The flare occurs in the inter-spot region, in a closed magnetic field configuration, which is clearly seen in the images of the upper and lower panels.

We also considered the M5.1 flare on September 28, 2014 accompanied by a CME occurring between two active regions, AR 12173 and AR 12172. They passed across the solar disk from September 21, 2014 to October 4, 2014 with a predominantly beta-gamma magnetic configuration, with AR 12172 producing 12 C flares and one M flare, while AR 12173 produced only one M flare.

Figure 8 shows the evolution of the magnetic field in AR 12173, EUV (131 and 94 Å) and radio emission (17 GHz) in intensity before and during the M5.1 flare on September 28, 2013 (T_{start} =02:32, T_{peak} = 02:43, T_{end} =

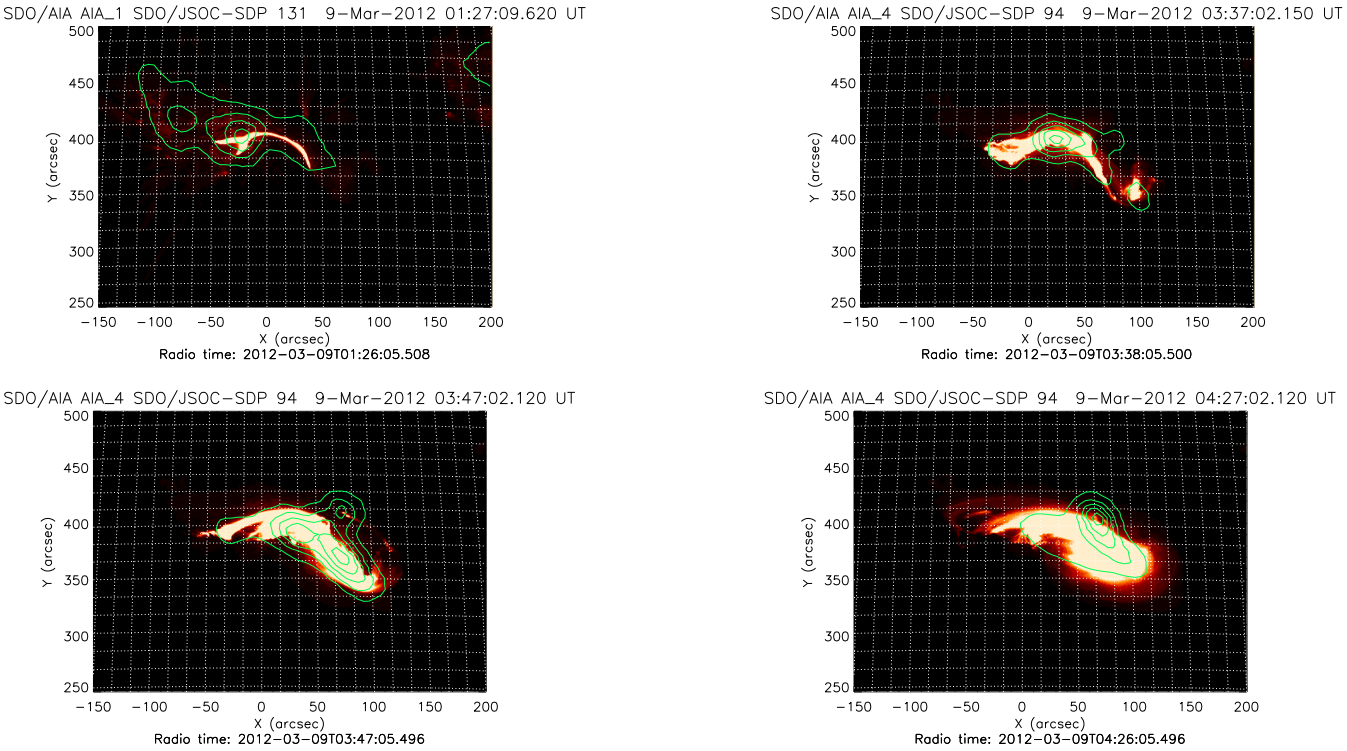

Fig. 5. Example of a sigmoid structure in AR 11429 on March 9, 2012. Overlay of radio emission intensity at a frequency of 17 GHz (I, contours) on the EUV map of 131 and 94 Å (background).

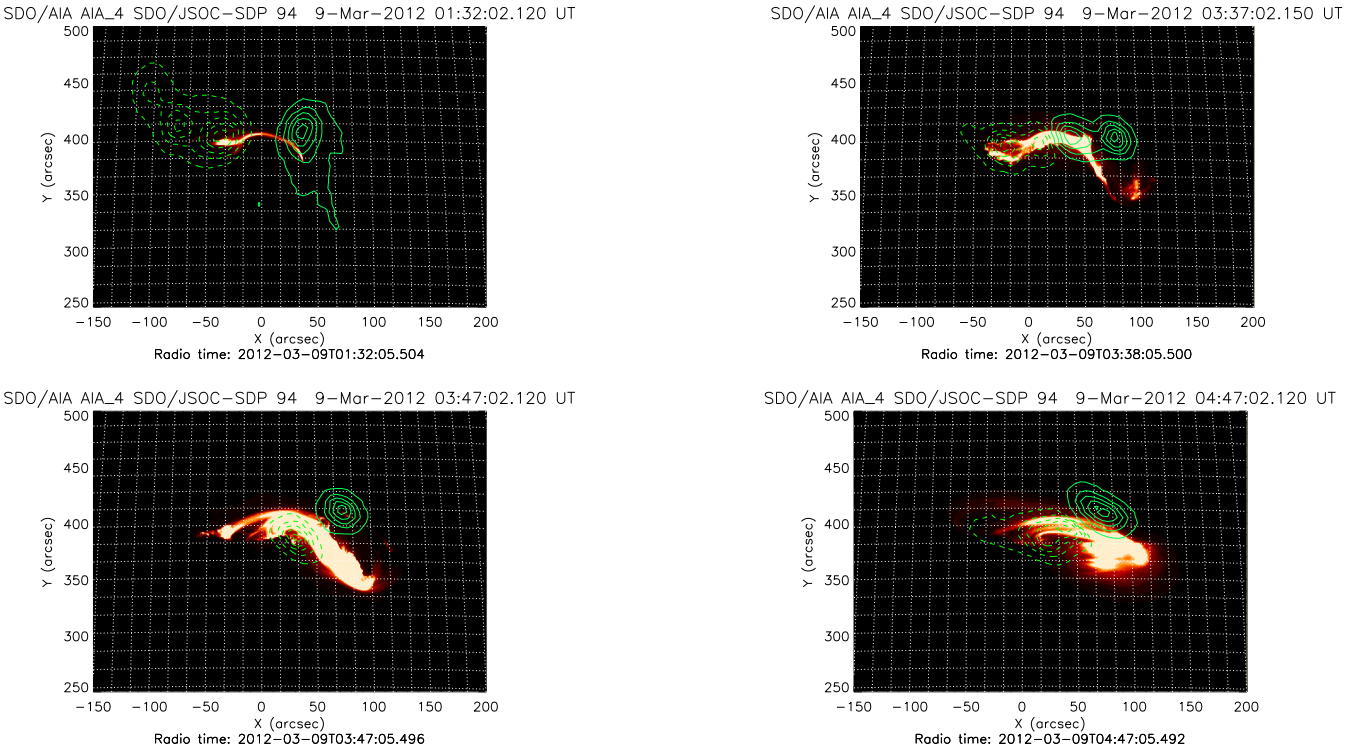

Fig. 6. Example of a sigmoid structure in AR 11429 on March 9, 2012. Overlay of circular polarization of radio emission at a frequency of 17 GHz (V, contours) on the EUV map of 94 Å (background).

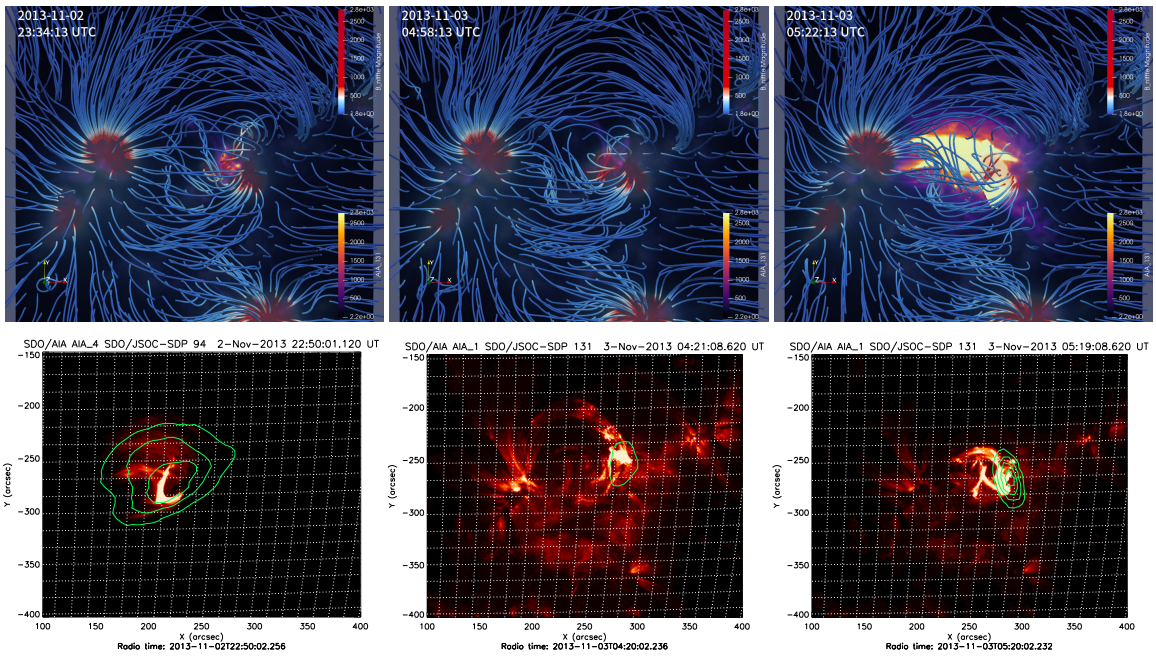

Fig. 7. Extrapolation of the magnetic field into the corona of AR 11884 (upper panel, lines) before and during the M4.9 flare on November 3, 2013 ($T_{\rm start}$ = 05:19, $T_{\rm peak}$ = 05:21, $T_{\rm end}$ = 06:30 UT). The magnitude of the magnetic field on the photosphere is shown by color (upper scale). The background shows the brightness of EUV emission in the 131 Å line (color, lower scale). The lower panel shows the overlay of radio emission at a frequency of 17 GHz in intensity (contours) on EUV images in the 94 and 131 Å lines (background).

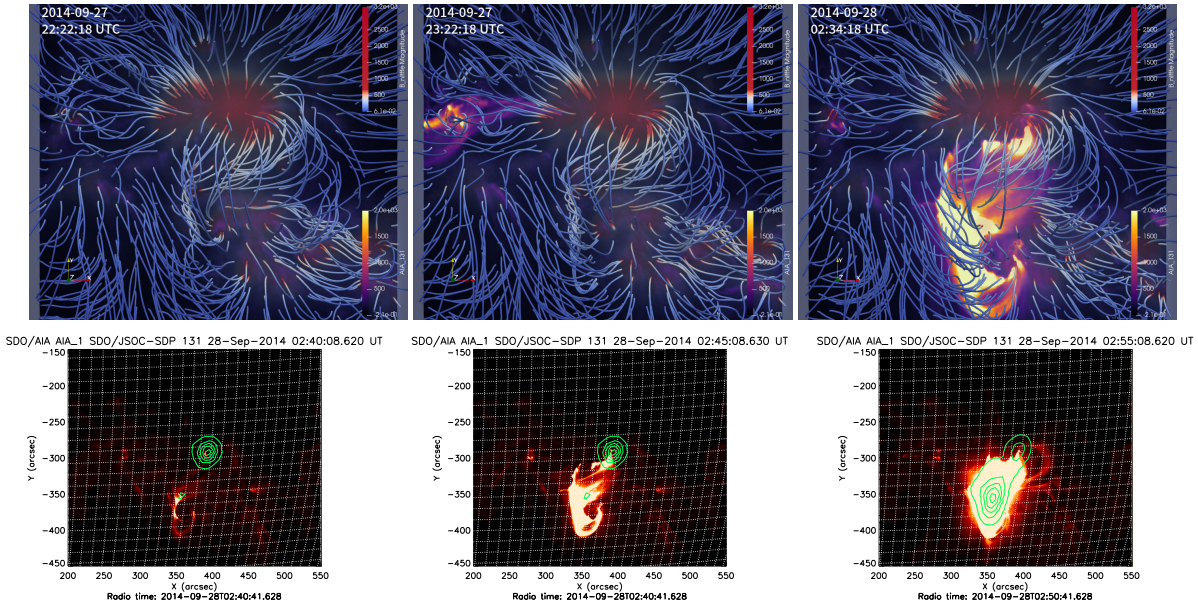

Fig. 8. Extrapolation of the magnetic field into the corona of AR 12173 (upper panel, lines) before and during the M5.1 flare on September 28, 2014 ($T_{\rm start}$ = 02:32, $T_{\rm peak}$ = 02:43, $T_{\rm end}$ = 03:24 UT). The magnitude of the magnetic field on the photosphere is shown by color (upper scale). The background shows the brightness of EUV emission in the 131 Å line (color, lower scale). The lower panel shows the overlay of radio emission at a frequency of 17 GHz in circular polarization (contours) on EUV images in the 94 and 131 Å lines (background).

03:24 UT) with a CME, also in a beta-gamma magnetic configuration, as in the first case considered. However, here the flare occurs in the southern part of AR 12173, in an open magnetic field configuration. The upper panels show that already 4 hours before the flare, in the place where it will occur (right upper panel), a twisted magnetic flux rope forms (left and middle panels). The lower panel shows the evolution of the radio source in intensity at a frequency of 17 GHz (contours) overlaid on EUV 131 Å. As can be seen, the magnetic flux rope formed to the south of the cyclotron source above the leading sunspot in AR 12173, where the maximum radio brightness is subsequently observed (lower right panel) and where the eruption probably occurs.

3 Conclusions

Based on observations from the Nobeyama Radio Heliograph (17 GHz), SDO/AIA, and SDO/HMI, we analyzed 16 active regions, 8 ARs of which had CMEs.

It was revealed that CMEs are predominantly initiated in events with open magnetic configurations, in the presence of twisted magnetic flux ropes, sigmoids, and emerging magnetic fluxes. The duration of flares, as well as the area of radio sources in the pre-flare phases, is on average larger in such events than in confined events.

Confined events are distinguished by the presence of a closed structure of field lines above the flare region (magnetic flux rope), which did not allow flare plasma to be ejected high into the corona.

This work was supported by the Russian Foundation for Basic Research and the Czech Science Foundation grant No. 20–52–26006.

References

Bakunina I.A., Melnikov V.F., 2019. Astron. Astrophys. Trans., vol. 31, no. 3, pp. 251–266.

Bakunina I.A., Melnikov V.F., Morgachev A.S., 2020a. Astrofizika, vol. 63, no. 2, pp. 252–259.

Bakunina I.A., Melnikov V.F., Morgachev A.S., 2020b. Geomagn. Aeron., vol. 60, no. 7, pp. 853–859.

Bakunina I.A., Melnikov V.F., Abramov-Maximov V.E, Morgachev A.S., 2021. Geomagn. Aeron., vol. 61, no. 8, pp. 1159–1171.

Canfield R.C., Hudson H.S., McKenzie D.E., 1999. Geophys. Research Lett., vol. 26, pp. 627–630.

Canfield R.C., Kazachenko M.D., Acton L.W., et al., 2007. Astrophys. J., vol. 671, pp. L81–L84.

Carmichael H., 1964. In Wilmot N.H. (Ed.), A process for flares. Washington, DC: National Aeronautics and Space Administration, Science and Technical Information Division, pp. 451–456.

Cheng X., Ding M.D., Zhang J., et al., 2014a. Astrophys. J., vol. 789, id. 93.

Cheng X., Ding M.D., Zhang J., et al., 2014b. Astrophys. Lett., vol. 789, id. L35.

Duan A., Jiang C., He W., et al., 2019. Astrophys. J., vol. 884, id. 73.

Hirayama T., 1974. Solar Phys., vol. 34, pp. 323–338.

Gibson S.E., Fan Y., Török T., Kliem B., 2006. Space Sci. Rev., vol. 124, pp. 131–144.

Kopp R.A., Pneuman G.W., 1976. Solar Phys., vol. 50, pp. 85–98.

Krista L.D., Reinard A., 2013. Astrophys. J., vol. 762, id. 91.

Manoharan P.K., van Driel-Gesztelyi L., Pick M., Demoulin P., 1996. Astrophys. Lett., vol. 468, pp. L73–L76.

Nindos A., Patsourakos S., Vourlidas A., Tagikas C., 2015. Astrophys. J., vol. 808, id. 117.

Romano P., Zuccarello F., Guglielmino S.L., 2015. Astron. Astrophys., vol. 582, article id. A55.

Rust D.M., Kumar A., 1996. Astrophys. Lett., vol. 464, pp. L199–L202.

Solov'ev A.A., Kirichek E.A., 2021. Mon. Not. Roy. Astron. Soc., vol. 505, pp. 4406–4416.

Sturrock P.A., 1966. Nature, vol. 211, pp. 695–697.

van Ballegooijen A.A., Martens P.C.H., 1989. Astrophys. J., vol. 343, pp. 971–984.

Wiegelmann T., 2004. Solar Phys., vol. 219, pp. 87–108.